

HiSAC: High-Resolution Sensing with Multiband Communication Signals

Jacopo Pegoraro[†], Jesus O. Lacruz^{*}, Michele Rossi[†], Joerg Widmer^{*}

[†]University of Padova, Italy, ^{*}IMDEA Networks Institute, Spain

ABSTRACT

Integrated Sensing And Communication (ISAC) systems are expected to perform accurate radar sensing while having minimal impact on communication. Ideally, sensing should only *reuse* communication resources, especially for spectrum which is contended by many applications. However, this poses a great challenge in that communication systems often operate on narrow subbands with low sensing resolution. Combining contiguous subbands has shown significant resolution gain in active localization. However, multiband ISAC remains unexplored due to communication subbands being highly sparse (*non-contiguous*) and affected by phase offsets that prevent their aggregation (*incoherent*). To tackle these problems, we design HiSAC, the first multiband ISAC system that combines diverse subbands across a wide frequency range to achieve super-resolved passive ranging. To solve the non-contiguity and incoherence of subbands, HiSAC combines them progressively, exploiting an anchor propagation path between transmitter and receiver in an optimization problem to achieve phase coherence. HiSAC fully reuses pilot signals in communication systems, it applies to different frequencies and can combine diverse technologies, e.g., 5G-NR and WiGig. We implement HiSAC on an experimental platform in the millimeter-wave unlicensed band and test it on objects and humans. Our results show it enhances the sensing resolution by up to 20 times compared to single-band processing while occupying the same spectrum.

1 INTRODUCTION

Endowing wireless communication systems with radar sensing capabilities is one of the key objectives of 3GPP Sixth Generation (6G) and future Wi-Fi [27]. In recent years, so-called Integrated Sensing And Communication (ISAC) systems have enabled a wide range of applications from multitarget tracking [34, 50], person identification [35, 55], activity recognition [23, 29], vital signs monitoring [57], pose estimation [10, 12], and object imaging [56, 61].

Motivation. A fundamental trade-off in ISAC systems is to achieve high sensing resolution, i.e., the capability of distinguishing multiple closely located targets, and accuracy with minimal impact on the primary communication functionality. Ideally, sensing should be performed by fully reusing resources available to the communication system

in time and frequency. Particular attention has to be put on spectrum, which is becoming more and more scarce due to the ubiquitous applications of Radio Frequency (RF) transmissions [41]. Indeed, ISAC benefits from using a large bandwidth since this is inversely proportional to the ranging resolution, i.e., the minimum signal propagation distance under which two targets can not be distinguished. However, the bandwidth available to existing communication systems is insufficient to achieve the desired *cm-level ranging* resolution in 6G. Even wideband Fifth Generation-New Radio (5G-NR) channels and IEEE 802.11ay (WiGig) in the Millimeter-Wave (mmWave) band can at most reach 37 cm and 17 cm resolution with 400 MHz and 1.76 GHz bandwidth, respectively. Such resolution can be improved by applying super-resolution algorithms based on Multiple Signal Classification (MUSIC) or Compressed Sensing (CS), e.g., [14, 16, 39], but the bandwidth limitation remains.

A possible solution to enhance the resolution is to *combine* multiple communication frequency bands to increase the sensing bandwidth. This approach has been attempted for active localization in Orthogonal Frequency Division Multiplexing (OFDM) systems (where the user carries a communication device) [16, 32, 48, 54], radar [6, 53, 65], and recently for sub-6 GHz Wi-Fi sensing in [49]. However, several limitations make the above methods unsuitable for ISAC. On the one hand, active localization approaches exploit either contiguous or closely-spaced subbands, which may not be available in ISAC since the spectrum is contended by a plethora of services and contains frequency gaps. Moreover, they can count on a *collaborative* localized device, which simplifies the problem since synchronization errors that prevent accurate delay measurements can be resolved via handshaking [14]. On the other hand, radar methods use dedicated waveforms, optimized for sensing purposes, and relatively wide subbands to be combined, which significantly simplifies the problem. Lastly, [49] employs a neural network model to overcome the above limitations in Wi-Fi, but this ties the system to the specific frequency band, communication technology (Wi-Fi), and hardware used to collect the training data. Conversely, we aim to develop a system that seamlessly adapts to OFDM, Single Carrier (SC), cellular, or Wi-Fi.

Challenges. Designing such a system presents several open challenges. First, one must tackle the non-contiguity of communication systems subbands, which may include gaps

of several hundreds of MHz or even GHz. Second, the different subbands are affected by time-varying and unknown timing, frequency, and phase offsets that prevent the coherent combination of the Channel Frequency Response (CFR) estimated by the communication protocol over different ISAC receivers (RXs) [51, 64]. Although the compensation of timing and frequency offsets in ISAC systems has been widely studied [22, 31, 33, 59, 66], *phase synchronization* is not well investigated since it is not needed in typical sensing tasks such as target tracking and Doppler estimation. On the contrary, achieving phase coherence is a strict requirement to combine multiple subbands over a wide frequency range. Third, communication subbands are relatively narrow with respect to the total bandwidth required to achieve high resolution. This makes it difficult to model individual subbands as they contain an insufficient number of frequency samples. Conversely, reconstructing the CFR over the total bandwidth entails huge computational complexity due to the high number of subcarriers. Finally, the designed method should generalize to different communication systems (OFDM vs. SC), protocols (5G-NR vs. Wi-Fi), and channel representations (e.g., CFR vs. Channel Impulse Response (CIR)).

Contribution. To address these challenges, we design and validate HiSAC, the first multiband ISAC system that fully reuses communication traffic across multiple bands (and technologies) to boost the sensing resolution, as shown in Fig. 1. HiSAC first combines all the subbands used by the same ISAC transmitter (TX)-RX pair (a *subsystem*), which are affected by the same offsets and hence phase-coherent. Then, it compensates for relative timing, frequency, and phase offsets across different subsystems, which are instead incoherent. For this, a new *phase synchronization* algorithm is proposed based on a simple, yet effective, initialization, based on an anchor propagation path, and refinement through an optimization problem. Then, HiSAC combines all the available subbands across subsystems with a focused Orthogonal Matching Pursuit (OMP) algorithm [8] that exploits the (coarse) prior knowledge about targets' locations obtained from the single subsystems, and outputs super-resolved range estimates. As a final step, HiSAC can combine range estimates obtained from different packets or OFDM slots *over time* (coherently or incoherently) to further boost the resolution and accuracy. Our approach combines subbands over several GHz of bandwidth, fully reusing pilot signal in communication systems, e.g., Synchronization Signal Blocks (SSBs) in 5G-NR, and applies to different frequencies, communication systems, and even different technologies, e.g., SC and OFDM.

We implement HiSAC on a Radio Frequency System on a Chip (RFSoc) platform in the mmWave unlicensed band (58-64 GHz). We demonstrate that HiSAC achieves a few-cm ranging resolution on metal and human targets, giving a 3 to 20 times improvement over baseline methods. Moreover, it

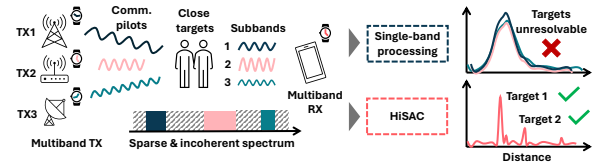


Figure 1: Overview of HiSAC's multiband sensing.

works in mono-/bi-static configurations on typical multiband systems employing Carrier Aggregation (CA), Bandwidth Part (BWP), and it is robust to target motion.

The contributions of our work can be summarized as:

1. We propose HiSAC, the first *multiband* ISAC system that achieves super-resolution passive ranging using non-contiguous, narrow, and incoherent subbands estimated by sets of communication pilot signals over time.
2. HiSAC features new model-based signal processing steps to achieve phase-coherence among subbands that adapt to different systems and technologies across GHz-wide bands.
3. Our approach entails zero additional overhead on communication and seamlessly integrates with multiband communication systems that adopt CA or BWP.
4. We prototype HiSAC in the unlicensed mmWave band and test it on a vast experimental campaign, showing it can achieve up to 20 times better resolution compared to a single band with the same spectrum occupation per time slot.

2 PRELIMINARIES

In this section, we provide useful background on the applicability of HiSAC in ISAC systems, ranging resolution, and phase incoherence due to phase offsets.

2.1 HiSAC use cases in ISAC

Multiband operation is widely used in communications to increase the data rate and multiplex applications to different users. In this section, we provide an overview of three practical use cases of our method for multiband ISAC: Two of them are typical of cellular networks, such as 5G-NR or future 6G, and one tackles cross-technology multiband sensing.

Carrier aggregation. CA is a function implemented in the Radio Access Network (RAN) and User Equipments (UEs) of 5G-NR mobile wireless networks. CA combines multiple frequency allocations (carriers) at different radio cells to boost the data rate of the connection [21]. A set of serving cells is identified that contributes to the aggregation, which can take place within the same frequency band (intra-band), e.g., within the sub-6 GHz range, or across multiple bands (inter-band), e.g., across Frequency Range (FR) 2 and FR 3. Exploiting the channel estimation process carried out on each frequency band for sensing would greatly enhance the available bandwidth and, as a result, the ranging resolution.

Bandwidth part. BWP is a mechanism to split the radio channel available to a cell into multiple segments (*parts*), which can then be used to allocate different regions of the spectrum to different applications (or UEs) [24]. Only one part can be active at a time, and SSBs can be transmitted in each part to synchronize to different UEs. Given that SSBs have a relatively narrow bandwidth, it is appealing to develop a system that can combine the SSBs transmitted by one or more radio cells to perform accurate mono-static ranging by exploiting the total frequency aperture over a wider bandwidth. Note that, BWP poses the additional requirement that the system must be able to operate with CFR estimates that are not collected simultaneously in all the subbands.

Cross-technology multiband processing. Coexistence of *unlicensed* 5G-NR and IEEE 802.11ay has been advocated in the 60 GHz band and has gathered significant interest from academia and industry [7, 36]. Flexible multiband processing across OFDM and SC communication technologies is appealing to boost sensing resolution in these cases. While combining multiple Wi-Fi channels has been studied for both communication [3] and localization [16, 54], combining multiple frequency bands obtained by Wi-Fi and cellular communication systems is still unexplored. In the mmWave band, IEEE 802.11ay channels span a wide bandwidth of 1.76 GHz, while in 5G-NR channels are limited to 400 MHz. Therefore, combining multiple channels across the two technologies can yield practical Ultra-Wide Band (UWB)-level resolution with CFR estimates spanning several GHz of bandwidth.

2.2 Delay and ranging resolution

The delay resolution, $\Delta\tau$, of a localization or passive sensing system is related to the bandwidth, B , of the transmission signal as $\Delta\tau = 1/B$. The corresponding ranging resolution for passive sensing also depends on the angle between the segments connecting the TX to the target and the target to the RX (*bi-static* angle), β , as $\Delta r = c/[2B \cos(\beta/2)]$. A mono-static system, with co-located TX and RX, gives $\Delta r = c/(2B)$ which minimizes Δr with respect to β . Unlike radar systems, which typically feature a large transmission bandwidth fully dedicated to sensing, communication systems are relatively narrowband for sensing purposes. As an example, even mmWave 5G-NR system with 400 MHz channels can only reach up to 37 cm mono-static ranging resolution, which may be insufficient for fine-grained sensing applications. Moreover, such resolution is only obtained if the full bandwidth is used to estimate the channel. This is often not the case, since pilot signals are transmitted on a subset of the available subcarriers. The SSBs used for synchronization with UEs, for example, occupy 240 OFDM subcarriers with at most 240 kHz subcarrier spacing. This leads to a very coarse ranging resolution of $\Delta r = c/(2 \cdot 240 \cdot 240\text{kHz}) = 2.6$ m.

Improving ranging resolution is a challenging task since the bi-static angle depends on the location of the TX, RX, and target, and increasing the bandwidth is not viable in ISAC systems since it is pre-determined by the communication protocol. Super-resolution approaches have been proposed that exploit subspace-based methods, e.g., MUSIC [16], or CS algorithms [15], exploiting assumptions on the structure of the channel (e.g., sparsity). However, none of these methods can drastically improve the ranging resolution, and limitations due to the narrow bandwidth remain.

2.3 Phase-incoherence among subbands

In a wireless communication system, the clock signal of each node is generated from a Local Oscillator (LO). The different LOs are asynchronous, meaning that, due to hardware non-idealities, they are subject to time-varying relative drifts from their nominal oscillating frequencies [63]. In addition, their initial phase is random. This introduces unwanted offsets in the received signals that are specific to each TX-RX pair. These can be categorized into Timing Offset (TO), Carrier Frequency Offset (CFO), and Random Phase Offset (RPO) [51].

TO results from the lack of time synchronization between the TX and RX. It is due to the unknown shift or offset affecting the RX clock relative to the TX one, and to the synchronization point chosen by the RX. TO is time-varying and causes an undesired phase term that increases linearly with the subcarriers in OFDM systems.

CFO is due to the time-varying difference in the LOs of the TX and RX. Communication systems typically estimate and partially compensate for the CFO. This leads to a residual CFO that is fast time-varying, as a result of the compensation error [51]. CFO causes a cumulative phase shift across packets or OFDM slots.

The RPO can be caused by non-idealities in the TX and RX devices, as well as by phase noise [37]. It varies on an OFDM symbol basis. Note that RPO can be present even between the multiple channels of the same LO.

When multiple ISAC systems in different frequency bands are considered, a direct combination of their CFRs is infeasible due to the presence of the above offsets. Indeed, this causes the phases of the CFRs in the different bands to be misaligned at the different RXs, preventing the construction of a common model spanning the full frequency band. Several approaches have been proposed to tackle TO and CFO in ISAC systems [4, 22, 29, 31, 33, 57–59, 66]. However, none of these tackles phase synchronization by also eliminating the RPO, which is essential for multiband CFR combination.

3 SYSTEM MODEL

In this section, we formulate a general model of a multiband ISAC system that fits all the use cases in Section 2.1.

3.1 Non-coherent subsystems and subbands

Consider a wide frequency band with bandwidth B and starting frequency f_0 , which we denote as the *full band* of interest, as shown in Fig. 2. We call Δ_f the spacing of the frequency samples of the considered CFR (subcarriers). Δ_f corresponds to the subcarrier spacing in OFDM systems or to the Discrete Fourier Transform (DFT) samples spacing used in SC systems. The total number of *virtual* subcarriers in the full band is $K = B/\Delta_f$, indexed by $k = 0, \dots, K - 1$. We use the term *virtual* to highlight that not all the subcarriers are used for communication, which is carried out on a subset of the full band spectrum. In the following, we assume the same subcarrier spacing Δ_f is shared by all the considered subbands, which can be achieved using interpolation or downsampling.

We consider an ISAC system consisting of C non-coherent subsystems affected by TO, CFO, and RPO. Each subsystem, i , includes one TX-RX pair that may be co-located (*mono-static*) or widely separated (*bi-static*). In practice, a subsystem can be represented by co-located Base Stations (BSs) or Access Points (APs) from different operators, acting as mono-static ISAC transceivers, or BS-BS/BS-UE pairs in the bi-static case. Subsystem i has bandwidth B_i , starting from frequency f_i , contained in the full band. The total number of virtual subcarriers of a subsystem is $K_i = B_i/\Delta_f$. Within each subsystem, the channel is estimated over a set S_i of potentially non-contiguous subbands, with $|S_i| = S_i$. The subbands may span the whole B_i or a part of it, according to the allocation of pilot signals used for channel estimation. We use index $s = 1, \dots, S_i$ to identify the subbands in subsystem i . Note that S_i may equal 1 if system i has a single subband. We call the total number of subbands in the system $S = \sum_{i=1}^C S_i$. Each subband contains a set of $K_{i,s}$ subcarriers. The subcarriers in the system for which the channel is estimated are called *available* subcarriers. The number of available subcarriers is $M_i = \sum_{s=1}^{S_i} K_{i,s}$, for subsystem i and $M = \sum_{i=1}^C M_i$ for the whole system, with $M_i \leq K_i$ and $M < K$.

Since each ISAC subsystem has a single RX, all the subbands of the same subsystem i share the same TO, CFO, and RPO due to being implemented on the same radio device. In our model, we consider TO, CFO, and RPO of subsystem i to be relative to the first subsystem ($i = 1$), which we take as a reference. Hence, we denote by $\tau_{o,i}(t)$, $f_{o,i}(t)$, and $\varphi_{o,i}(t)$ the relative TO, CFO, and RPO of subsystem i , respectively. The absolute offsets do not impact the performance of our system and are omitted in the model.

3.2 Multiband channel model

In this section, we present the multiband CFR model. We consider a time-varying multipath channel with L propagation paths, where t is used to denote time. We denote by $\tau_l(t)$

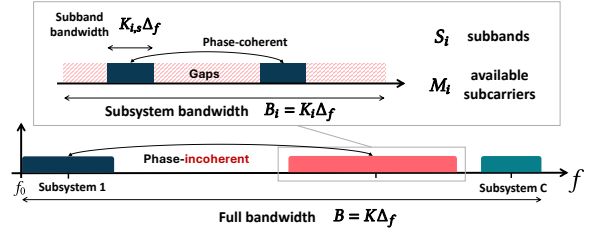


Figure 2: Summary of subsystems and subbands notation.

and $\alpha_l(t)$ the delay of the l -th channel path due to propagation and its complex amplitude at time t , accounting for the combined effect of the propagation loss and the target's scattering phase [38].

We model the CFR over the full band, discretized by the subcarrier spacing Δ_f . The expression of the full band CFR for subcarrier k at time t is

$$H_k(t) = \sum_{l=1}^L \alpha_l(t) e^{-j2\pi k \Delta_f \tau_l(t)}, \quad k = 0, \dots, K - 1, \quad (1)$$

with delay resolution $\Delta\tau = 1/(\Delta_f K)$. The CIR can be obtained from the CFR via an Inverse DFT (IDFT) along the subcarriers. Note that, in Eq. (1), we include the carrier phase into each path's complex amplitude $\alpha_l(t)$. Considering the carrier phase in the fullband channel model would lead to high sensitivity of the algorithm to errors in the positioning of the TX and RX antennas of each subsystem, which would make it impractical to use. This is especially true for at mmWave frequencies where the wavelength is short. Hence, HiSAC exploits the bandwidth aperture B , rather than the carrier f_0 . As commonly done in the UWB channels literature [46, 47], we consider the coefficients $\alpha_l(t)$ to be constant within the frequency band of interest. This holds if the total bandwidth is less than 20% of the carrier frequency [30].

We denote by $k_{i,s}$ the starting index of subband s in subsystem i in the full band grid, $k = 0, \dots, K$. The CFR in subband s , at subcarrier $\kappa = 0, \dots, K_{i,s} - 1$, is

$$H_{i,s,\kappa}(t) = e^{j\phi_{o,i}(t)} e^{-j2\pi\kappa\Delta_f\tau_{o,i}(t)} \sum_{l=1}^L \alpha_l(t) e^{-j2\pi(k_{i,s}+\kappa)\Delta_f\tau_l(t)}, \quad (2)$$

where $\phi_{o,i}(t) = -2\pi f_{o,i}(t)t + \varphi_{o,i}(t)$ is denoted by Phase Offset (PO) in the following. The PO contains the contribution of the CFO and the RPO since these are constant in κ and l .

4 HISAC METHODOLOGY

This section presents HiSAC's processing steps, which are summarized in the following and shown in Fig. 3.

(1) Coherent intra-subsystem combination. The first step performs a coarse multiband reconstruction of the CFR, using only the coherent subbands in each subsystem, as detailed in Section 4.1. The reason to first aggregate subbands over

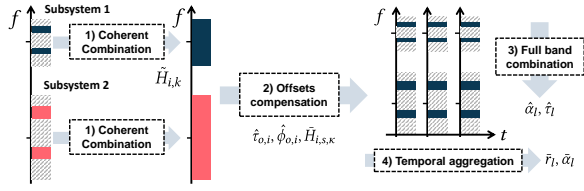


Figure 3: HiSAC high-level overview.

each subsystem is to obtain a wider-band CFR, to simplify the subsequent removal of phase offsets.

(2) TO and PO compensation. This step applies a new algorithm to achieve phase synchronization across multiple subsystems, making them suitable for coherent multiband combination (see Section 4.2). Compared to existing approaches, ours is more robust with narrow, non-contiguous subbands by (i) exploiting an anchor path for TO initialization and (ii) accurately estimating TO and PO via optimization.

(3) Inter-subsystem multiband reconstruction. Delays and amplitudes of the multipath components in the CFR are estimated using all the available subbands. This is done with the OMP algorithm, to tackle the gaps in the CFR measurements, by restricting the search space around the initial estimates obtained from the coherent subsystems to counter the discretization error, as detailed in Section 4.3.

(4) Temporal aggregation. HiSAC can optionally aggregate the estimates of the multipath parameters across time, represented by different packets or OFDM slots. The aggregation consists of an accumulation and selection algorithm, that yields significantly improved ranging accuracy and resolution after a few time slots (see Section 4.4).

Steps (1)-(3) do not depend on the time instant in which the CFR is estimated, so we omit the time t in their description.

4.1 Intra-subsystem coherent combination

As a first step, we combine the subbands obtained by each subsystem i coherently (since they experience the same TO and PO) to coarsely estimate the multipath delays and complex amplitudes. To do so, we use the OMP algorithm [8], which leverages the sparsity of the CIR in the delay domain resulting from the limited number of propagation paths. OMP operates on a grid of candidate path delays, which can be tuned according to the availability of computational resources. We set up a grid with Q_i candidates as $0, \dots, (Q_i - 1)\delta_i$, where δ_i is the grid granularity of subsystem i . Then, we construct a partial Fourier matrix, \mathbf{F}_i , that spans all the subcarriers in subsystem i and the delays in the grid. Element m, q of \mathbf{F}_i is $(\mathbf{F}_i)_{m,q} = e^{j2\pi m q \delta_i \Delta_f} / \sqrt{K_i}$. Denote by \mathbf{A}_i the matrix whose rows are the vectors of all zeros but the k -th component, which equals 1, with $k \in \{k_{i,1}, \dots, K_{i,1} - 1, \dots, k_{i,S}, \dots, K_{i,S} - 1\}$. We use \mathbf{A}_i to select the rows of \mathbf{F}_i whose indices are in the set of available CFR samples in subsystem i . Call $\mathbf{\Gamma}_i = \mathbf{A}_i \mathbf{F}_i$, and define $\mathbf{H}_i = [H_{i,1,0}, \dots, H_{i,1,K_{i,1}-1},$

$\dots, H_{i,S,0}, \dots, H_{i,S,K_{i,S}-1}]^T$, that contains all the CFR measurements in subsystem i . We denote by \mathbf{h}_i the coarse CIR estimate obtained by fusing the S_i subbands. The following model holds, $\mathbf{H}_i = \mathbf{\Gamma}_i \mathbf{h}_i + \mathbf{w}_i$, where $\mathbf{w}_i \sim \mathcal{CN}(0, \sigma_w^2 \mathbf{I})$ is a complex noise vector. Call $\|\cdot\|_0$ the number of non-zero components of a vector. OMP solves the following problem iteratively,

$$\mathbf{h}_i = \arg \min_{\mathbf{h}} \|\mathbf{h}\|_0 \text{ s. t. } \|\mathbf{H}_i - \mathbf{\Gamma}_i \mathbf{h}\|_2^2 < \epsilon, \quad (3)$$

to retrieve the sparsest estimate of the CIR that leads to a bounded Mean Squared Error (MSE) with the CFR measurements. The bound on the MSE is regulated by the positive constant ϵ , estimated from the noise level in the CFR estimates. We stop the execution of OMP once the reconstruction error falls below 5% of the norm of \mathbf{H}_i .

We call L_i^{OMP} the number of non-zero components of \mathbf{h}_i . OMP yields the set of paths delays and complex amplitudes, which we denote by $\{\alpha_{i,l}, \tau_{i,l}\}_{l=1}^{L_i^{\text{OMP}}}$. These correspond to the values and locations of the non-zero elements of vector \mathbf{h}_i in the grid. Note that $\tau_{i,l}$ is an estimate of $\tau_{1,l} + \tau_{o,i}$, i.e., the delays $\tau_{i,l}$ contain the relative TO. Finally, a synthetic CFR for subsystem i , is obtained as $\tilde{H}_{i,k} = \sum_{l=1}^{L_i^{\text{OMP}}} \alpha_{i,l} e^{-j2\pi k \Delta_f \tau_{i,l}}$, where k can be extended even outside of the subsystems' bandwidth. This will be used in the next section to compensate for relative TOs and Frequency Offsets (FOs).

4.2 Relative TO and PO compensation

In the second step, the relative TOs and POs among the different ISAC subsystems are compensated for. This is done by leveraging an *anchor* propagation path between the TX and the RX of each subsystem since the TO and PO are common to all paths [63]. The anchor path could be either the Line-of-Sight (LOS) path, which is commonly assumed to be available in ISAC [64], or a non-LOS static path seen by all subsystems. In the following, we first cast the TO and PO estimation as an optimization problem. Then, we detail how to exploit the anchor path in different subsystems to initialize the TO accurately. Finally, we solve the optimization and compensate for TO and PO to achieve phase-coherence.

Problem formulation. We compensate for $\tau_{o,i}$ and $\phi_{o,i}$ using the synthesized CFR of subsystem i and that of the reference subsystem. TO and PO can be estimated by solving the following minimization problem

$$\begin{aligned} \{\hat{\tau}_{o,i}, \hat{\phi}_{o,i}\} &= \arg \min_{\tau, \phi} \sum_{k=0}^{K-1} \left| \tilde{H}_{1,k} - e^{-j\phi} e^{j2\pi k \Delta_f \tau} \tilde{H}_{i,k} \right|^2 \\ &= \arg \min_{\tau, \phi} \sum_{k=0}^{K-1} -2\text{Re} \left\{ e^{-j\phi} e^{j2\pi k \Delta_f \tau} \tilde{H}_{1,k}^* \tilde{H}_{i,k} \right\}, \end{aligned} \quad (4)$$

where $*$ and $\text{Re}\{\cdot\}$ are the complex conjugate and real part of a complex number, respectively. Eq. (4) is high-dimensional,

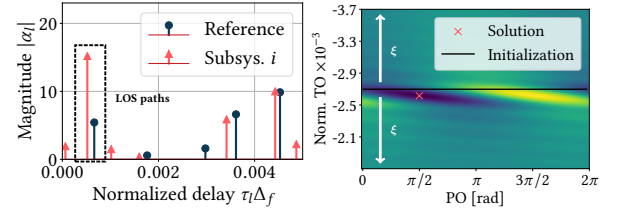
non-linear, and non-convex, which causes solvers to converge to inaccurate solutions and get stuck in local minima. Moreover, its computational complexity is prohibitive since the number of frequency samples K is huge due to its relation with the subcarrier spacing.

Initialization. To solve the problem, we obtain an accurate initial estimate of the TO from the synthesized CFRs. We select the anchor path delay for subsystem i , denoted by $\tau_{i,1}$, among $\{\alpha_{i,l}, \tau_{i,l}\}_{l=1}^{L_i^{\text{OMP}}}$. If this corresponds to the LOS, it is easily identifiable by having strong received power compared to scattered paths [18] and by having the smallest propagation delay. If the anchor path is a non-LOS static reflection, it can be localized by each subsystem before applying HiSAC. For the reference subsystem, $\tau_{1,1}$ is not affected by relative TO. Hence, we estimate the latter as the difference between the anchor path delay of subsystem i and that of the reference subsystem, $\hat{\tau}'_{o,i} = \tau_{i,1} - \tau_{1,1}$. This reasoning is shown in Fig. 4a. Initializing the TO estimate using delay differences is an innovation of HiSAC. It allows reducing the complexity of directly solving Eq. (4) by reducing the search space for the TO which, unlike the PO, is unbounded and causes fast oscillations of the cost function.

Refinement. Once the initial estimate of the TO has been obtained, we refine it by solving Eq. (4). The computational complexity is greatly reduced by searching over a small neighborhood of $\hat{\tau}'_{o,i}$, while for the PO we search over the interval $[0, 2\pi]$. We use a grid search for this optimization, focusing the search space in $[\hat{\tau}'_{o,i} - \xi, \hat{\tau}'_{o,i} + \xi]$ for the TO, where $\xi = 5\delta_i$, i.e., 5 times the OMP grid step of the subsystem. We use a grid spacing of $2\xi/100$ for TO and $\pi/100$ for PO. As a result, we obtain estimates of the TO, $\hat{\tau}_{o,i}$, and PO, $\hat{\phi}_{o,i}$. Fig. 4b shows an example of the refinement step.

TO and PO compensation. The TO and PO are compensated for in each subband by using their estimates as $\bar{H}_{i,s,k} = e^{-j\hat{\phi}_{o,i}} e^{j2\pi\hat{\tau}_{o,i}k\Delta_f} H_{i,s,k}$. This enables the coherent combination of the subbands across the full band of interest.

Remark. The proposed method can handle CFR estimates obtained at different time instants by the different subsystems, as long as the time difference among the estimates is short enough to consider the channel parameters to be constant. To see this, consider Eq. (2) and two CFR estimates obtained by subsystems 1 and 2 at times t_1 and t_2 , respectively. If the two estimates are sufficiently close in time, the channel parameters α_l and τ_l can be considered constant. Conversely, the offsets $\tau_{o,2}(t)$, $\phi_{o,2}(t)$ are fast time-varying, so they change from t_1 to t_2 . Taking subsystem 1 at time t_1 , our approach compensates for the cumulative TO and PO, given by $\tau_{o,2}(t_2) + \tau_{o,2}(t_1)$ and $\phi_{o,2}(t_2) + \phi_{o,2}(t_1)$. HiSAC is therefore general enough to handle relative TO and PO due to collecting CFR at different time instants. This feature makes it extremely flexible in utilizing the CFR estimates



(a) Delay difference of the anchor paths initializes the TO. (b) Cost function, yellow/blue represent high/low values.

Figure 4: Example estimation of the initialization value for the TO, (a), and the refinement via optimization, (b).

obtained by the communication system. Moreover, compared to methods based on linear fitting of the unwrapped phase at different subcarriers, e.g., [16, 54], our approach is more effective with non-contiguous frequency bands (see Section 6).

4.3 Multiband fusion

Once the available subbands have been made mutually coherent, we use OMP to obtain a combined set of delay estimates. Given the large number of subcarriers, K , in the total bandwidth, a direct application of OMP would either have prohibitive computational complexity if we select a small grid spacing, or give inaccurate results if the grid spacing is too large. To solve this issue, we leverage the knowledge of the delays estimated by the single subsystems before the coherent fusion to greatly reduce the search space. This can be thought of as focusing the OMP algorithm around the solutions obtained from the lower-resolution subsystems.

Consider the reference subsystem and denote by $\{\tau_{1,l}\}_{l=1}^{L_1^{\text{OMP}}}$ its set of delays. HiSAC first obtains a union of intervals around the candidate delays from the reference subsystem, i.e., $\mathcal{R} = \bigcup_l \mathcal{R}_l$, where $\mathcal{R}_l = [\tau_{1,l} - \gamma, \tau_{1,l} + \gamma]$. γ is chosen as half the best nominal delay resolution among the subsystems, i.e., $\gamma = 1/(2 \max_i(B_i))$. Then, HiSAC discretizes \mathcal{R} to construct a grid of Q candidate delays for OMP with step δ . The elements of the discretized set of delays are denoted by v_1, \dots, v_Q . A partial $K \times Q$ Fourier matrix, \mathbf{F} is constructed with the discretized delays, giving $(\mathbf{F})_{k,q} = e^{j2\pi k v_q \Delta_f} / \sqrt{K}$. Denote by \mathbf{A} the selector matrix whose rows are the \mathbf{e}_k , $k \in \{k_{1,1}, \dots, K_{1,1} - 1, \dots, k_{C,S}, \dots, K_{C,S} - 1\}$ the matrix that selects the rows of \mathbf{F} whose indices are in the set of available CFR samples. Call $\mathbf{\Gamma} = \mathbf{A}\mathbf{F} \in \mathbb{C}^{M \times Q}$, and define the CFR vector of dimension M

$$\bar{\mathbf{H}} = [\bar{H}_{1,1,0}, \dots, \bar{H}_{1,1,K_1}, \dots, \bar{H}_{C,S,0}, \dots, \bar{H}_{C,S,K_S}]^T, \quad (5)$$

that contains all the available measurements from all the S subbands. We denote by $\mathbf{h} \in \mathbb{C}^Q$ the CIR obtained by fusing the S subbands. Using OMP we estimate \mathbf{h} by solving the same problem in Eq. (3), using $\bar{\mathbf{H}}$ as the measurement vector and $\mathbf{\Gamma}$ as the model matrix. As for the single subsystems,

OMP is stopped once the reconstruction error with respect to the measurements reaches a 5% threshold, and the corresponding number of non-zero components of $\hat{\mathbf{h}}$ is L^{OMP} . The set of path delays and amplitudes obtained from the non-zero components of $\hat{\mathbf{h}}$ is $\{\hat{\alpha}_l, \hat{\tau}_l\}_{l=1}^{L^{\text{OMP}}}$. The delays are then mapped to relative distances as $\hat{r}_l = c\hat{\tau}_l - D$, where D is the distance between the TX to the RX, assumed known. Relative distances can be used to localize a target in both mono-static and bi-static scenarios, as described, e.g., in [18, 33, 34].

4.4 Temporal aggregation

In this section, we discuss how HiSAC can improve its ranging accuracy and resolution by aggregating multiple channel estimates across time, as detailed in Alg. 1.

Consider a sequence of N path delays, $\{\hat{\tau}_1(t_n), \dots, \hat{\tau}_{L^{\text{OMP}}}(t_n)\}_{n=1}^N$, and amplitudes, $\{\hat{\alpha}_1(t_n), \dots, \hat{\alpha}_{L^{\text{OMP}}}(t_n)\}_{n=1}^N$, obtained by applying HiSAC to different ISAC packets or OFDM slots. These must be obtained in a short processing interval such that the underlying channel parameters can be considered constant. Recall that the delays outputted by OMP belong to a discrete grid of candidates v_q , with $q = 1, \dots, Q$, which is kept fixed during the aggregation period. The temporal aggregation step is based on the following observation: When applied over a short time interval where the channel is almost constant, HiSAC outputs correlated sets of delays that can be aggregated (coherently or incoherently). To do so, Alg. 1 proceeds by first iterating over the elements in the delay grid and over time slots (line 2). Then, if v_q is among the set of outputs of OMP in the considered slot n , we aggregate it to a running average of the path amplitudes, χ_q (lines 3-5). We propose two alternative versions of the algorithm for static targets and human sensing (line 4), respectively. If the targets are static, the temporal aggregation can be performed by taking into account the phase of the complex amplitudes (coherent aggregation), which gives higher Signal-to-Noise Ratio (SNR) and resolution. With dynamic targets such as humans instead, we only aggregate the magnitude information for each path (incoherent aggregation) since the time variation of the phase due to respiration or slight movement would lead to destructive interference. Finally, in line 13, we select as the final improved set of delays the L^{OMP} candidates for which χ_q is highest, which we denote by $\bar{\tau}_l$, for $l = 1, \dots, L^{\text{OMP}}$. The channel gains of such delays are the corresponding χ_q , which we call $\bar{\alpha}_l$. The delays are then mapped to relative distances as $\bar{r}_l = c(\bar{\tau}_l - \bar{\tau}_1)$.

5 IMPLEMENTATION

To implement HiSAC, we use the open-source Mimorph platform [20] as a baseline. The platform includes an AMD

Algorithm 1 HiSAC multipath temporal aggregation.

Input: Set of delays and amplitudes across time $\hat{\tau}_l(t_n), \hat{\alpha}_l(t_n)$, for $l = 1, \dots, L^{\text{OMP}}$ and $n = 1, \dots, N$, OMP grid v_1, \dots, v_Q , order L^{OMP} .
Output: Improved set of delays and amplitudes.
1: Initialize $q = 1, \chi_q = 0, \forall q = 1, \dots, Q$.
2: **for** $q = 1, \dots, Q$ and $n = 1, \dots, N$ **do**
3: **if** $v_q \in \{\hat{\tau}_l(t_n)\}_{l=1}^{L^{\text{OMP}}}$ **then**
4: $\chi_q \leftarrow \begin{cases} [\hat{\alpha}_l(t_n) + n\chi_q] / (n+1) & \text{if target is static,} \\ [|\hat{\alpha}_l(t_n)| + n\chi_q] / (n+1) & \text{otherwise.} \end{cases}$
5: **end if**
6: **end for**
7: Keep the L^{OMP} path delays with the highest χ_q , with delays v_q .

(Xilinx) RFSoc that comprises Field Programmable Gate Array (FPGA) logic, multiple AD/DA converters, and high-performance ARM processors. We implement HiSAC to work in the unlicensed 58-64 GHz mmWave band using linear antenna array front-ends with 16 elements from Sivers Semiconductors, suitable for analog beamforming. We choose a mmWave frequency band as it represents a challenging test case, given the high sensitivity to CFO and the strong phase noise of high frequencies [37]. Signal conditioning from the RFSoc to the mmWave front-ends includes DC-block filters, low-pass filters (1 GHz cut-off frequency), and 3 dB attenuators. The main components of a TX-RX node of the testbed are shown in Fig. 5a. We configure the testbed to work as $C = 2$ incoherent subsystems with carrier frequencies 60.48 GHz and 62.64 GHz. The testbed can operate concurrently as TX and RX, in mono-static configuration, or as a bi-static system, using two nodes like the one in Fig. 5a.

Signal generation. Signals for each sub-system are generated offline. Evaluating HiSAC requires collecting full band CFR estimates and other information used as ground truth, as detailed in Section 6.1. Therefore, we generate a composite packet including 5G-NR OFDM symbols and IEEE 802.11ay channel estimation fields. An OFDM symbol including Demodulation-Reference Signal (DM-RS), spanning the full bandwidth, is used as ground truth (see the *Full band* baseline in Section 6.1). An IEEE 802.11ay Channel Estimation Field (CEF) is used for SC CIR estimation. 5G-NR pilot signals spanning different subbands are used for HiSAC, with bandwidth and starting frequency depending on the specific experiment. The signal is sent to the RFSoc using an Ethernet port and stored in loopback memories implemented in the FPGA logic. The FPGA clock is set to 245.76 MHz with a super-sampling rate factor of 8, giving an equivalent of 1966.08 MHz. The Inter-Frame Spacing (IFS) is configurable in runtime by a host PC. Since more than one subsystem is employed, independent data paths are used and connected to independent mmWave front-ends (Fig. 5a).

Signal capture and saving. To enable the testbed operation in mono-/bi-static operation, we modify the packet

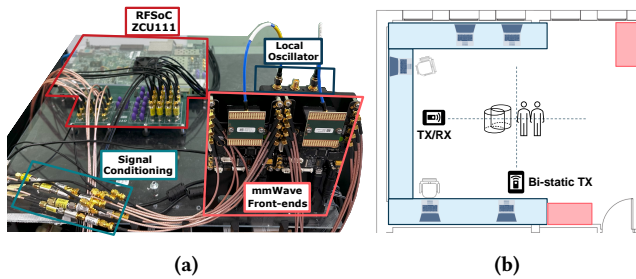


Figure 5: HiSAC prototype (a) and experimental environment (b).

detection block from [19] to either trigger packet capture when detecting a valid preamble in bi-static operation mode or trigger the capture when transmitting a packet (mono-static mode). The operating mode can be updated at runtime from a host PC. Valid packets are stored in on-board RAM (up to 4GB) and then these are offloaded through a 10 Gb Ethernet interface to be processed offline.

6 EXPERIMENTAL RESULTS

In this section, we describe the experimental setup used in the evaluation of HiSAC. Then we provide an in-depth analysis of our results obtained in different settings.

6.1 Experiments and baselines

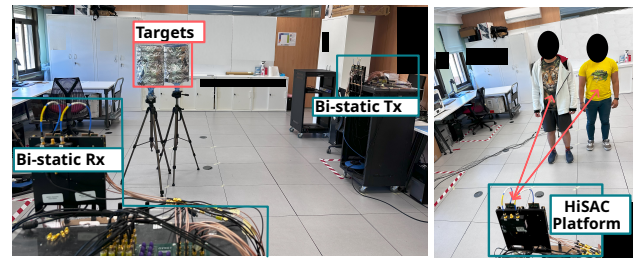
Experiments description. To evaluate HiSAC, we perform 27 experiments involving ISAC radio channel measurements in different scenarios and configurations. Each experiment is repeated 5 times and involves the transmission of 100 packets with an IFS of 50 ms (unless stated otherwise). The experiments are carried out indoors, in a 7 m × 6 m room (see Fig. 5b), and can be divided into six groups detailed in the following. In groups (1)-(5) we use metal cylindrical reflectors as targets, while group (6) involves human subjects. Groups (1)-(4) and (6) are obtained in a mono-static scenario, while in (5) we use a bi-static setting. As anchor path to achieve phase coherence we use the self-interference path in the mono-static scenario and the LOS in the bi-static one.

(1) *2 targets (8 experiments)*: 2 metal cylinders are placed at different distances from the system, ranging from 1.5 to 5 m. The inter-target distance is changed from 30 cm to 60 cm.

(2) *3 targets (5 experiments)*: 3 metal cylinders are placed at different distances from the system, ranging from 2 to 5 m. The inter-target distance is changed from 30 cm to 60 cm.

(3) *Resolution limit test (3 experiments)*: 2 metal cylinders are placed at 17.2, 10.1, and 3.1 cm inter-target distance, to evaluate the maximum resolution achieved by HiSAC. The distance of the second target from the TX is 2.78 m.

(4) *Changing angle (5 experiments)*: 2 metal cylinders are placed about 2.5 m from the TX with 33 cm inter-target distance. We change the angular location of the targets in



(a) Bi-static setup.

(b) Human sensing.

Figure 6: Experiments in the bi-static setting and with static subjects.

different experiments among -30° , -15° , 17° , 30° . In each, experiment, we change the antenna Beam Pattern (BP) used by the TX to point at the targets. This scenario is of high practical interest since pilot signals transmitted in ISAC systems (e.g. SSBs) are often beamformed in different directions.

(5) *Bi-static scenario*: This group of experiments is performed in a bi-static scenario with a distance of 3.24 m between the TX and the RX. 2 metal cylinders are placed close to each other so that the segments connecting the TX to the target, and the target to the RX form a 90° angle (bi-static angle). The inter-target bi-static distance changes in different experiments from 3.5 cm to 8.9 cm. This scenario is particularly challenging since the nominal ranging resolution in the bi-static case is degraded by a factor of 0.7 due to the 90° bi-static angle, as shown in Section 2.2.

(6) *Human localization and tracking*: A final group of experiments is performed with human targets, to demonstrate the effectiveness of HiSAC on weaker multipath components with respect to metal reflectors and its robustness to movement. These involve (i) 2 static subjects standing at 2.30 and 2.64 m from the TX as shown in Fig. 6b, (ii) 2 moving targets walking back and forth from 3 to 1 m from the TX (in this case, the IFS is reduced to 5 ms). Experiments involving people have been carried out in compliance with the IRB of our institute and do not disclose information about the subjects.

Baselines for comparison. Since HiSAC is the first method to perform multiband ISAC, we evaluate it against the baseline methods described in the following. Note that [49], which is the closest prior work, is not suitable for comparison since (i) it is based on a deep neural network trained on sub-6 GHz signals, so it would need extensive data collection and retraining on our implementation, (ii) it uses a channel hopping scheme to collect CFR samples that is specific to sub-6 GHz Wi-Fi and does not apply to 5G-NR.

Laser telemeter. We collect ground truth distance measurements of the targets using a laser telemeter, mounted on the TX-RX antenna front-end.

Full band. We collect CFR measurements over an equivalent bandwidth to the full band of interest and use OMP to obtain target distance estimates. This is a benchmark to assess how

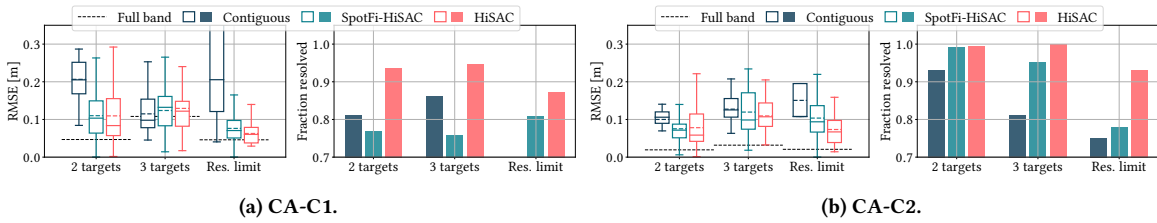


Figure 7: HiSAC results in the CA-C1/C2 setting. We report the ranging RMSE and the FRT in experiment groups (1)-(3).

close HiSAC gets to the performance of a wideband ISAC system with a bandwidth equal to its total virtual bandwidth. *Contiguous band*. We collect CFR measurements over a *contiguous* region of the spectrum with a bandwidth equal to the real bandwidth of HiSAC, which includes only the subcarriers in which the channel is measured. OMP is then used to obtain distance estimates.

SpotFi-based HiSAC (SpotFi-HiSAC). To demonstrate the effectiveness of HiSAC’s algorithm to achieve phase coherence across subbands, we design a competitor algorithm that uses SpotFi’s approach, [16], to perform this task. The rest of the delay estimation process is the same as in HiSAC, since the original SpotFi uses MUSIC to estimate delays which does not apply to non-contiguous subbands. SpotFi’s approach uses line fitting on the unwrapped phase of the CFR, then matches such models across the subbands, compensating for the differences in the slopes and intercepts.

Evaluation metrics. We adopt two main metrics to evaluate HiSAC. The first one is the Root Mean Squared Error (RMSE) in the distance estimation, computed with respect to the laser telemeter distance measurement. RMSE can only be computed for the targets that are detected by the algorithm, and it is undefined for unresolved targets. Therefore, we introduce a second metric which we call Fraction of Resolved Targets (FRT). This represents the fraction of targets that an algorithm can resolve, i.e., detect correctly, with respect to the total number of targets resolved by the full band baseline. We consider a target to be correctly detected by an algorithm if this outputs a target distance sufficiently close, i.e., closer than the minimum inter-target distance in the experiment, to the laser telemeter ground truth distance for that target. The two metrics should be jointly considered in each evaluation since an algorithm may yield a very low RMSE but have low resolution, which means it is not exploiting the increased bandwidth. Conversely, an algorithm could have high resolution but poor accuracy, giving a high RMSE.

6.2 In-depth evaluation

In this section, we evaluate HiSAC in the three use cases from Section 2.1, using the experiments from Section 6.1.

Carrier Aggregation. We start our evaluation with the CA scenario, combining multiple 5G-NR channels with 100

and 400 MHz bandwidth. We assume that in this case the CFR is estimated over the full channels, similar to using DM-RS pilots that span the full bandwidth [43]. We consider two configurations with 2 subsystems:

(i) Configuration 1 (CA-C1), including 4 subbands with an effective bandwidth of 400 MHz and a virtual bandwidth of 2.01 GHz. The first two subbands belong to subsystem 1, while the second two to subsystem 2. The starting frequencies of the subbands relative to the first one are $\{0, 0.19, 1.63, 1.91\}$ GHz, while their bandwidths are all equal to 100 MHz;

(ii) Configuration 2 (CA-C2), including 5 subbands with an effective bandwidth of 800 MHz and a virtual bandwidth of 3.46 GHz. The first three subbands belong to subsystem 1, while the second two to subsystem 2. The starting frequencies of the subbands relative to the first one are $\{0, 0.19, 1.2, 2.88, 3.36\}$ GHz, while their bandwidths are $\{0.1, 0.1, 0.4, 0.1, 0.1\}$ GHz.

The main challenge in the CA scenario is to effectively combine subbands that are widely separated in the spectrum. Fig. 7 shows the RMSE and FRT obtained by HiSAC in experiment groups (1)-(3) with the CA use case. The horizontal dashed line represents the average RMSE obtained using the full band CFR. With CA-C1, HiSAC achieves accurate ranging with an average RMSE below 15 cm in all the experiments. The case with 3 targets gives the highest average RMSE due to the higher complexity of the multipath environment. The contiguous bandwidth and SpotFi-HiSAC yield comparable or worse RMSE. This proves that HiSAC gains ranging accuracy thanks to the increased virtual bandwidth and outperforms SpotFi’s method to achieve phase coherence. In terms of FRT, HiSAC provides significant gains. In the resolution limit test, the contiguous band is unable to resolve the targets (0.5 FRT), while HiSAC gives 0.93 FRT. With CA-C2, the overall performance in terms of RMSE and FRT on 2 and 3 targets improves for all methods due to the wider virtual bandwidth. However, only HiSAC significantly benefits from such increased virtual bandwidth when considering the resolution limit test, achieving higher FRT compared to CA-C1, while other methods perform slightly worse.

Bandwidth Part. Next, we analyze a BWP scenario, where we combine multiple CFR estimates obtained by a 5G-NR system using SSB signals, spanning 240 subcarriers in the

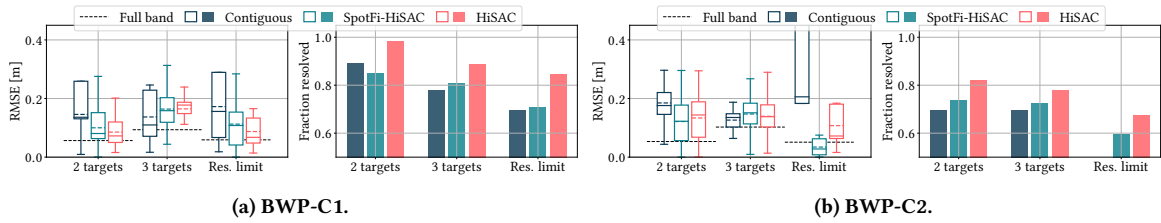


Figure 8: HiSAC results in the BWP-C1/C2 setting. We report the ranging RMSE and the FRT in experiment groups (1)-(3).

middle of the operating channel. Note that here the bandwidth of each subband is significantly lower than in the CA case since the CFR is measured only on a fraction of the total communication channel. Specifically, using 240 KHz subcarrier spacing, which is reasonable at mmWave frequencies, the bandwidth of each SSB is $B_{i,s} = 57.6$ MHz. We consider two different configurations with 2 subsystems:

(i) Configuration 1 (BWP-C1), including 4 subbands with an effective bandwidth of 460.8 MHz and a virtual bandwidth of 1.267 GHz. The first four subbands belong to subsystem 1, while the second four to subsystem 2. The starting frequencies of the subbands relative to the start of the full band are $\{0.02, 0.12, 0.22, 0.32, 0.91, 1.01, 1.11, 1.21\}$ GHz;

(ii) Configuration 2 (BWP-C2), including 5 subbands with an effective bandwidth of 230.4 MHz and a virtual bandwidth of 1.267 GHz. The first two subbands belong to subsystem 1, while the second two to subsystem 2. The starting frequencies of the subbands relative to the start of the full band are $\{0.02, 0.12, 0.91, 1.01\}$ GHz.

We stress that, as required by BWP operation, each CFR estimate in different subbands is obtained at a different time instant, with an IFS of 50 ms. Hence, the spectrum occupied at each time instant is just 57.6 MHz. An example result on BWP-C1 is shown in Fig. 9, reporting the CFR and CIR squared magnitude (Power-Delay Profile (PDP)). The main challenge in the BWP scenario is to combine narrow available subbands due to the use of unmodified SSB pilot signals. Fig. 8 shows the RMSE and FRT obtained by HiSAC in the experiment groups (1)-(3) with the BWP use case. With BWP-C1, HiSAC outperforms the other approaches. Note that with 3 targets it achieves slightly higher mean RMSE with respect to the contiguous band (2 cm), but has a higher FRT by 0.1. BWP-C2 represents a very challenging scenario due to the sparsity of the available spectrum (amounting to 18% of the virtual bandwidth) and to the narrow subbands used. In the resolution limit test, the contiguous CFR method fails in resolving the targets and has large RMSE, while HiSAC achieves 11 cm average RMSE and 0.67 FRT, with a resolution gain of 13% over SpotFi-HiSAC.

Cross-technology evaluation. To demonstrate the flexibility of HiSAC, we evaluate it in a cross-technology scenario where we combine a 400 MHz 5G-NR OFDM channel, with

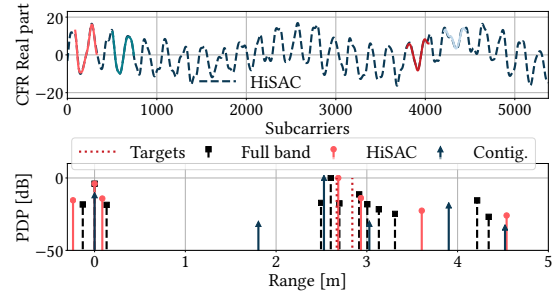


Figure 9: Example HiSAC results in BWP-C2. The top plot shows the subbands after coherency has been achieved and the reconstructed HiSAC CFR. The bottom plot shows the PDP.

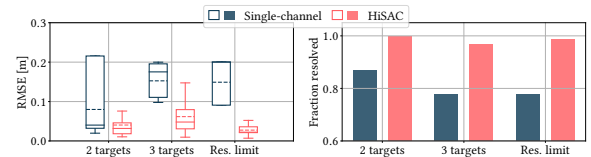


Figure 10: Cross-technology HiSAC results.

carrier frequency 59.69 GHz, with a 1.76 GHz IEEE 802.11ay SC channel (WiGig) with carrier frequency 62.64 GHz. The virtual bandwidth in this configuration is 4.03 GHz, while the available one is 2.16 GHz. Note that, in SC systems, the CIR is estimated directly via cross-correlation with the transmitted pilot signals. Therefore, before applying HiSAC, we convert the IEEE 802.11ay CIR into the CFR using a DFT. In Fig. 10, we show the RMSE and FRT results in the cross-technology scenario. As a comparison, we use the targets detected by the peaks of the CIR estimated by a single IEEE 802.11ay channel. HiSAC obtains extremely accurate ranging with an average RMSE of at most 5 cm (3 targets), whereas the single channel has a worst-case RMSE of 15 cm. In terms of FRT, HiSAC gives an almost identical resolution to the full bandwidth, with a worst-case FRT of 0.95 with three targets.

Impact of angle and beamforming. ISAC systems apply beamforming to direct the signal towards the communication RX or targets. HiSAC is robust to such changes in the direction of the transmission, as demonstrated by our results in Fig. 11, obtained on experiments from group (4). The target ranging RMSE remains below 15 cm when changing the

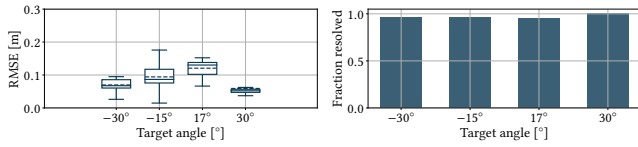


Figure 11: HiSAC results changing target angle and transmission BP.

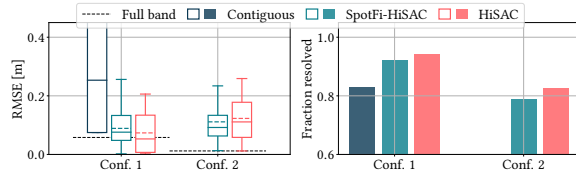


Figure 12: HiSAC results in a bi-static BWP scenario.

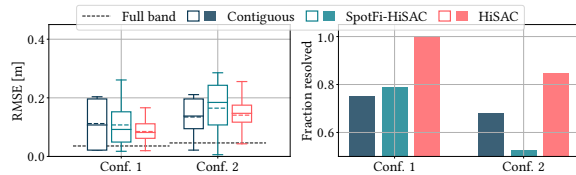


Figure 13: HiSAC results with human subjects using BWP.

angle from -30° to 30° . The FRT does not change significantly when changing the transmission angle, proving that HiSAC can accurately measure distances in different directions.

Bi-static setting. We evaluate HiSAC’s capability to estimate the targets’ distances in a bi-static setting, using experiments from group (5) and the BWP-C1/C2 configurations. Note that the full band range resolution in this case is reduced to $\Delta r = c/(2B \cos(\pi/4)) \approx 17.5$ cm due to the bi-static angle being 90° . Fig. 12 shows the RMSE and FRT obtained by HiSAC in the bi-static setting. These results are comparable to those obtained in the mono-static setting with a similar configuration, proving that HiSAC works when the TX and RX are widely separated. Conversely, the contiguous CFR can not resolve the targets with BWP-C2.

People localization. We test HiSAC on human subjects to demonstrate its capability to resolve weaker reflections, using the experiments from group (6). Fig. 13 shows the RMSE and the FRT. These results are obtained using the BWP-C1 and C2 configurations. HiSAC achieves 8 and 15 cm average RMSE with C1 and C2, respectively. Moreover, the FRT gain that it provides with respect to using the contiguous CFR is large: 0.25 using C1 and 0.17 using C2. Note that SpotFi-HiSAC’s FRT with human subjects degrades much more than HiSAC’s one. Being based on an anchor path, our method to achieve phase coherence is *independent* of the strength of the target multipath component.

People tracking. Fig. 14 shows the PDP across time obtained from the CIR estimated by HiSAC and with the full band with 2 subjects walking back and forth. Peaks in

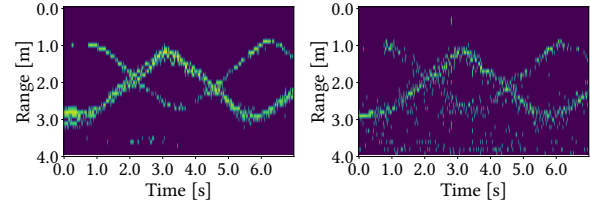


Figure 14: Tracking 2 subjects across time in the BWP-C1 scenario. We plot the normalized PDP obtained from the reconstructed CIR with the full band (left) and HiSAC (right). HiSAC’s resolution is comparable to that of the full 1.2 GHz bandwidth.

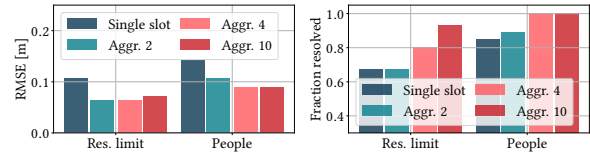


Figure 15: Improvement due to the temporal aggregation (Alg. 1) on experiments (3), Resolution limit, and (6), People, using BWP-C2.

the PDP (in yellow) correspond to the subjects. Although HiSAC’s PDP is noisier than that of the full band, its resolution, i.e., the capability of distinguishing the two subjects across time, is comparable. The bandwidth used by HiSAC in each time slot is only 57.6 MHz (20 times lower than the full bandwidth) corresponding to a resolution of 2.6 m.

Temporal aggregation improvement. Fig. 15 shows the RMSE and FRT results obtained by aggregating HiSAC’s range estimates over 2, 4, or 10 time slots using Alg. 1. This evaluation is carried out on the most challenging scenarios we considered during the evaluation, namely BWP-C2 and groups of experiments (3) and (6). Our results demonstrate the effectiveness of temporal aggregation, which improves RMSE by around 30% and FRT by up to 0.25 with respect to single-slot HiSAC.

7 RELATED WORK

Super-resolution wireless sensing. Subspace-based super-resolution methods [17] and CS [8] are widely used in radar and ISAC, but are still limited by the transmission bandwidth. Some of their recent applications to ISAC are found in [25, 60]. Other approaches have employed the spatial diversity of the RX array [61] to perform high-resolution imaging in the mmWave band, but they can not be applied to low-cost systems with a single RF chain such as analog beamforming systems. In [28, 40], a novel approach to apply distributed Synthetic Aperture Radar (SAR) techniques to vehicular sensing systems is introduced. This approach boosts the resolution by combining distributed devices, thus requiring multiple cooperating nodes. HiSAC instead *reuses* the frequency diversity of communication systems without

additional requirements. Notably, HiSAC could be combined with any of the above techniques to enhance their resolution.

Multiband radar sensing. Multiband sensing has been studied in the radar literature. [6] has first proposed bandwidth interpolation between two subbands to increase ranging resolution via Auto-Regressive (AR) modeling and non-linear optimization. Other works have followed a similar research direction adopting different algorithms for combining the subbands [9, 11, 42, 44, 53, 62, 65]. The above works are based on radar systems, which adopt optimized chirp waveforms and can rely on wide individual subbands. This significantly simplifies the problem with respect to an ISAC setting where CFR estimates are not under control and can be very narrow, which makes radar approaches underperform. To solve this problem, HiSAC innovates with a progressive combination of subbands over coherent subsystems first, and then over the full band of interest.

OFDM-based multiband processing. Several works have demonstrated that combining multiple frequency bands can boost the resolution of OFDM systems in active localization. In [16, 52, 54], SpotFi, Splicer, and ToneTrack are presented, which combine (*stitch*) multiple contiguous or overlapping Wi-Fi subbands to increase the multipath resolution. To eliminate phase offsets, they use linear fitting of the unwrapped phase, which is prone to errors when used on non-contiguous, narrow subbands spanning several GHz. Other Wi-Fi-based approaches [14, 15, 45] have tackled the same problem but rely on a handshaking process between TX and RX to eliminate phase offsets, which does not apply to passive sensing in ISAC. [13, 32, 47, 48] propose alternative algorithms based on maximum-likelihood. All these approaches target active localization, in which the RX device is the localized target. HiSAC instead localizes targets from backscattered reflections, as done by radar systems.

More recently, [46] has brought the research attention to exploiting multiband CFR to perform wideband radar-like ranging in ISAC. To the best of our knowledge, the only system that tackles this problem is UWB-Fi [49], in the sub-6 GHz unlicensed spectrum. However, this system is based on a neural network that learns to combine subbands and compensate for phase offsets. Changing hardware, frequency band, or technology (OFDM vs SC) may require retraining the system which is time-consuming and requires new data. Conversely, HiSAC does not require training and generalizes to different implementations.

Cross-band channel prediction. A recent line of work has investigated channel prediction in one frequency band from an available channel estimate in a different band [1, 2, 5, 21, 26]. Although the general idea of this problem is linked to the multiband setting, predicting the channel in a different band is significantly different from combining multiple non-contiguous incoherent CFR estimates to increase the

total system bandwidth. Moreover, the above works focus on communication, hence the channel prediction is mostly aimed at estimating SNR at the RX. Conversely, HiSAC is an ISAC system that estimates fine-grained complex amplitudes and delays of individual paths in the channel.

8 DISCUSSION AND LIMITATIONS

Sensing over very large bandwidth. HiSAC can aggregate subbands over regions of the spectrum spanning several GHz. However, aggregation between very far frequency bands (e.g., sub-6 GHz and mmWave) is not feasible, since the frequency-dependency of the scattering coefficients of the different paths would become non-negligible and prevent coherent aggregation. Future research in this direction is key to truly exploit the multiband potential.

Impact of the scattering angle. The phase of the scattering coefficients $\alpha_l(t)$ in Eq. (2) is assumed to be approximately constant for all subsystems. This assumption holds for isotropic targets or if the scattering angle is similar across subsystems [28]. This assumption is reasonable for ISAC BSs and APs that are typically clustered on the same antenna poles. Combining spatially diverse subsystems across multiple bands will be investigated in future work.

Impact of narrow subbands. In the limit case in which each HiSAC subsystem estimates a single very narrow subband, reconstructing a subsystem-wide CFR model could be challenging. If targets are too close to the TX, the CFR may not oscillate fast enough to have sufficient information about the path delay in the narrow subband. This is a challenging problem that requires further investigation.

Impact of Doppler. The impact of Doppler on subbands combination remains unexplored in ISAC. Due to its variation with carrier frequency, Doppler introduces a path- and subsystem-specific phase shift on the CFR which may degrade the subbands combination. HiSAC is sufficiently robust to this phenomenon as shown in Section 6.2. However, further investigation of this aspect is required.

9 CONCLUSION

The problem of achieving range super-resolution in ISAC systems with narrow and discontinuous subbands is addressed in this paper. To solve it, we present HiSAC, a general signal-processing method for coherent multiband ranging that enhances the resolution of existing communication systems by only reusing channel estimates obtained via pilot signals. Our approach does not rely on a specific hardware or protocol and works across different communication technologies (i.e., 5G-NR or IEEE 802.11ay). Our extensive experiments with objects and humans demonstrate that HiSAC enhances the resolution by up to 20 times compared to single-band processing, occupying the same bandwidth in each time slot.

REFERENCES

- [1] Arjun Bakshi, Yifan Mao, Kannan Srinivasan, and Srinivasan Parthasarathy. 2019. Fast and Efficient Cross Band Channel Prediction Using Machine Learning. In *The 25th Annual International Conference on Mobile Computing and Networking (Los Cabos, Mexico) (MobiCom '19)*. Association for Computing Machinery, New York, NY, USA, Article 37, 16 pages.
- [2] Avishek Banerjee, Xingya Zhao, Vishnu Chhabra, Kannan Srinivasan, and Srinivasan Parthasarathy. 2024. HORCRUX: Accurate Cross Band Channel Prediction. In *Proceedings of the 30th Annual International Conference on Mobile Computing and Networking (Washington D.C., DC, USA) (ACM MobiCom '24)*. Association for Computing Machinery, New York, NY, USA, 1–15.
- [3] Sergio Barrachina-Muñoz, Boris Bellalta, and Edward W Knightly. 2021. Wi-Fi channel bonding: An all-channel system and experimental study from urban hotspots to a sold-out stadium. *IEEE/ACM Transactions on Networking* 29, 5 (2021), 2101–2114.
- [4] Xu Chen, Zhiyong Feng, J Andrew Zhang, Xin Yuan, and Ping Zhang. 2023. Kalman Filter-based Sensing in Communication Systems with Clock Asynchronism. *IEEE Transactions on Communications* (2023).
- [5] Kun Woo Cho, Marco Cominelli, Francesco Gringoli, Joerg Widmer, and Kyle Jamieson. 2023. Scalable Multi-Modal Learning for Cross-Link Channel Prediction in Massive IoT Networks (*MobiHoc '23*). Association for Computing Machinery, New York, NY, USA, 221–229. <https://doi.org/10.1145/3565287.3610280>
- [6] Kevin M Cuomo, Jean E Pion, and Joseph T Mayhan. 1999. Ultrawideband coherent processing. *IEEE Transactions on Antennas and Propagation* 47, 6 (1999), 1094–1107.
- [7] Anastasia Daraseliya, Maksym Korshykov, Eduard Sopin, Dmitri Moltchanov, Sergey Andreev, and Konstantin Samouylov. 2021. Coexistence Analysis of 5G NR Unlicensed and WiGig in Millimeter-Wave Spectrum. *IEEE Transactions on Vehicular Technology* 70, 11 (2021), 11721–11735.
- [8] Yonina C Eldar and Gitta Kutyniok. 2012. *Compressed sensing: theory and applications*. Cambridge University Press.
- [9] Bilal Hussain, Antonio Malacarne, Salvatore Maresca, Filippo Scotti, Paolo Ghelfi, and Antonella Bogoni. 2018. Auto-regressive spectral gap filling algorithms for photonics-based highly sparse coherent multi-band radars in complex scenarios. In *2018 IEEE Radar Conference (RadarConf18)*. IEEE, 0993–0998.
- [10] Sijie Ji, Xuanye Zhang, Yuanqing Zheng, and Mo Li. 2024. Construct 3D Hand Skeleton with Commercial WiFi. In *Proceedings of the 21st ACM Conference on Embedded Networked Sensor Systems (<confloc>, <city>Istanbul</city>, <country>Turkiye</country>, </confloc>) (SenSys '23)*. Association for Computing Machinery, New York, NY, USA, 322–334.
- [11] Li Jia and Xiaojian Xu. 2006. A new procedure for ultra wideband radar imaging from sparse subband data. In *2006 8th international Conference on Signal Processing*, Vol. 4. IEEE.
- [12] Wenjun Jiang, Hongfei Xue, Chenglin Miao, Shiyang Wang, Sen Lin, Chong Tian, Srinivasan Murali, Haochen Hu, Zhi Sun, and Lu Su. 2020. Towards 3D human pose construction using wifi. In *Proceedings of the 26th Annual International Conference on Mobile Computing and Networking (London, United Kingdom) (MobiCom '20)*. Association for Computing Machinery, New York, NY, USA, Article 23, 14 pages.
- [13] Tarik Kazaz, Gerard JM Janssen, Jac Romme, and Alle-Jan Van der Veen. 2021. Delay estimation for ranging and localization using multiband channel state information. *IEEE Transactions on Wireless Communications* 21, 4 (2021), 2591–2607.
- [14] Mahdi Barzegar Khalilsarai, Benedikt Gross, Stelios Stefanatos, Gerhard Wunder, and Giuseppe Caire. 2020. WiFi-based channel impulse response estimation and localization via multi-band splicing. In *GLOBECOM 2020-2020 IEEE Global Communications Conference*. IEEE, Taipei, Taiwan.
- [15] Mahdi Barzegar Khalilsarai, Stelios Stefanatos, Gerhard Wunder, and Giuseppe Caire. 2019. WiFi-based indoor localization via multi-band splicing and phase retrieval. In *2019 IEEE 20th International Workshop on Signal Processing Advances in Wireless Communications (SPAWC)*. IEEE, Cannes, France.
- [16] Manikanta Kotaru, Kiran Joshi, Dinesh Bharadia, and Sachin Katti. 2015. SpotFi: Decimeter Level Localization Using WiFi. *SIGCOMM Comput. Commun. Rev.* 45, 4 (aug 2015), 269–282. <https://doi.org/10.1145/2829988.2787487>
- [17] Sun-Yuan Kung, K Si Arun, and DV Bhaskar Rao. 1983. State-space and singular-value decomposition-based approximation methods for the harmonic retrieval problem. *JOSA* 73, 12 (1983), 1799–1811.
- [18] Heiner Kuschel, Diego Cristallini, and Karl Erik Olsen. 2019. Tutorial: Passive radar tutorial. *IEEE Aerospace and Electronic Systems Magazine* 34, 2 (2019), 2–19.
- [19] Jesus O. Lacruz, Dolores Garcia, Pablo Jiménez Mateo, Joan Palacios, and Joerg Widmer. 2020. mm-FLEX: An Open Platform for Millimeter-Wave Mobile Full-Bandwidth Experimentation. In *ACM MobiSys'20*.
- [20] Jesus O. Lacruz, Rafael Ruiz, and Joerg Widmer. 2021. A Real-Time Experimentation Platform for sub-6 GHz and Millimeter-Wave MIMO Systems. In *ACM MobiSys'21*.
- [21] Qianru Li, Zhehui Zhang, Yanbing Liu, Zhaowei Tan, Chunyi Peng, and Songwu Lu. 2023. CA++: Enhancing Carrier Aggregation Beyond 5G. In *Proceedings of the 29th Annual International Conference on Mobile Computing and Networking (MobiCom '23)*. Association for Computing Machinery, New York, NY, USA, Article 5, 14 pages.
- [22] Xinyu Li, J Andrew Zhang, Kai Wu, Yuanhao Cui, and Xiaojun Jing. 2022. CSI-ratio-based Doppler frequency estimation in integrated sensing and communications. *IEEE Sensors Journal* (2022).
- [23] Guiping Lin, Weiwei Jiang, Sicong Xu, Xiaobo Zhou, Xing Guo, Yujun Zhu, and Xin He. 2023. Human Activity Recognition Using Smartphones With WiFi Signals. *IEEE Transactions on Human-Machine Systems* 53, 1 (2023), 142–153.
- [24] Xingqin Lin, Dongsheng Yu, and Henning Wiemann. 2021. *A Primer on Bandwidth Parts in 5G New Radio*. Springer International Publishing. https://doi.org/10.1007/978-3-030-58197-8_12
- [25] Yongjun Liu, Guisheng Liao, Yufeng Chen, Jingwei Xu, and Yingzeng Yin. 2020. Super-Resolution Range and Velocity Estimations With OFDM Integrated Radar and Communications Waveform. *IEEE Transactions on Vehicular Technology* 69, 10 (2020), 11659–11672.
- [26] Zikun Liu, Gagandeep Singh, Chenren Xu, and Deepak Vasishth. 2021. FIRE: enabling reciprocity for FDD MIMO systems. In *Proceedings of the 27th Annual International Conference on Mobile Computing and Networking (New Orleans, Louisiana) (MobiCom '21)*. Association for Computing Machinery, New York, NY, USA, 628–641. <https://doi.org/10.1145/3447993.3483275>
- [27] Shihang Lu, Fan Liu, Yunxin Li, Kecheng Zhang, Hongjia Huang, Jiaqi Zou, Xinyu Li, Yuxiang Dong, Fawang Dong, Jia Zhu, et al. 2024. Integrated sensing and communications: Recent advances and ten open challenges. *IEEE Internet of Things Journal* (2024).
- [28] Marco Manzoni, Dario Tagliaferri, Stefano Tebaldini, Marouan Mizmizi, Andrea Virgilio Monti-Guarnieri, Claudio Maria Prati, and Umberto Spagnolini. 2023. Wavefield networked sensing: Principles, algorithms and applications. *arXiv preprint arXiv:2305.10333* (2023).
- [29] Francesca Meneghello, Domenico Garlisi, Nicolò Dal Fabbro, Ilenia Tinnirello, and Michele Rossi. 2022. SHARP: Environment and Person Independent Activity Recognition with Commodity IEEE 802.11 Access

- Points. *IEEE Transactions on Mobile Computing* (2022).
- [30] Andreas F Molisch. 2009. Ultra-wide-band propagation channels. *Proc. IEEE* 97, 2 (2009), 353–371.
- [31] Zhitong Ni, J Andrew Zhang, Xiaojing Huang, Kai Yang, and Jinhong Yuan. 2021. Uplink sensing in perceptive mobile networks with asynchronous transceivers. *IEEE Transactions on Signal Processing* 69 (2021), 1287–1300.
- [32] Matteo Noschese, Fulvio Babich, Massimiliano Comisso, and Chris Marshall. 2020. Multi-band time of arrival estimation for long term evolution (LTE) signals. *IEEE Transactions on Mobile Computing* 20, 12 (2020), 3383–3394.
- [33] Jacopo Pegoraro, Jesus O Lacruz, Tommy Azzino, Marco Mezzavilla, Michele Rossi, Joerg Widmer, and Sundeep Rangan. 2024. JUMP: Joint communication and sensing with Unsynchronized transceivers Made Practical. *IEEE Transactions on Wireless Communications* (2024).
- [34] Jacopo Pegoraro, Jesus O Lacruz, Francesca Meneghello, Enver Bashirov, Michele Rossi, and Joerg Widmer. 2023. RAPID: Retrofitting IEEE 802.11ay access points for indoor human detection and sensing. *IEEE Transactions on Mobile Computing* (2023).
- [35] Jacopo Pegoraro, Jesus O Lacruz, Michele Rossi, and Joerg Widmer. 2022. SPARCS: A Sparse Recovery Approach for Integrated Communication and Human Sensing in mmWave Systems. In *2022 21st ACM/IEEE International Conference on Information Processing in Sensor Networks (IPSN)*. IEEE, 79–91.
- [36] Qualcomm. 2020. *5G unlicensed shared spectrum*. <https://www.qualcomm.com/research/5g/5g-unlicensed-shared-spectrum>.
- [37] Maryam Eslami Rasekh, Mohammed Abdelghany, Upamanyu Madhows, and Mark Rodwell. 2019. Phase noise analysis for mmwave massive MIMO: a design framework for scaling via tiled architectures. In *Conference on Information Sciences and Systems (CISS)*.
- [38] Mark A Richards, Jim Scheer, William A Holm, and William L Melvin. 2010. *Principles of modern radar*. Scitech Publishing Inc., Raleigh, NC, USA.
- [39] Piotr Samczyński, Karol Abratkiewicz, Marek Plotka, Tomasz P Zieliński, Jacek Wszolek, Sławomir Hausman, Piotr Korbel, and Adam Ksieżyk. 2021. 5G Network-Based Passive Radar. *IEEE Transactions on Geoscience and Remote Sensing* 60 (2021), 1–9.
- [40] Dario Tagliaferri, Marco Manzoni, Marouan Mizmizi, Stefano Tebaldini, Andrea Virgilio Monti-Guarnieri, Claudio Maria Prati, and Umberto Spagnolini. 2024. Cooperative Coherent Multistatic Imaging and Phase Synchronization in Networked Sensing. *IEEE Journal on Selected Areas in Communications* (2024).
- [41] Paolo Testolina, Michele Polese, Josep M. Jornet, Tommaso Melodia, and Michele Zorzi. 2024. Modeling Interference for the Coexistence of 6G Networks and Passive Sensing Systems. *IEEE Transactions on Wireless Communications* (2024), 1–1. <https://doi.org/10.1109/TWC.2024.3360628>
- [42] Jihua Tian, Jinping Sun, Guohua Wang, Yanping Wang, and Weixian Tan. 2013. Multiband radar signal coherent fusion processing with IAA and apFFT. *IEEE Signal Processing Letters* 20, 5 (2013), 463–466.
- [43] 3GPP TS38.300. 2018. NR and NG-RAN Overall Description; Stage 2 (Release 15). *V15.2.0 (2018-06)* (2018).
- [44] Philip van Dorp, Rob Ebeling, and Albert G Huizing. 2010. High resolution radar imaging using coherent multiband processing techniques. In *2010 IEEE Radar Conference*. IEEE, 981–986.
- [45] Deepak Vasisht, Swarun Kumar, and Dina Katabi. 2016. Decimeter-Level localization with a single WiFi access point. In *13th USENIX symposium on networked systems design and implementation (NSDI 16)*. 165–178.
- [46] Yubo Wan, Zhixiang Hu, An Liu, Rui Du, Tony Xiao Han, and Tony Q. S. Quek. 2024. OFDM-Based Multiband Sensing For ISAC: Resolution Limit, Algorithm Design, and Open Issues. *IEEE Vehicular Technology Magazine* 19, 2 (2024), 51–59.
- [47] Yubo Wan, An Liu, Rui Du, and Tony Xiao Han. 2022. Fundamental Limits and Optimization of Multiband Sensing. *arXiv preprint arXiv:2207.10306* (2022).
- [48] Yubo Wan, An Liu, Qiyu Hu, Mianyi Zhang, and Yunlong Cai. 2023. Multiband delay estimation for localization using a two-stage global estimation scheme. *IEEE Transactions on Wireless Communications* (2023).
- [49] Xin Li1 Hongbo Wang, Zhe Chen, Zhiping Jiang, and Jun Luo. 2024. UWB-Fi: Pushing Wi-Fi towards Ultra-wideband for Fine-Granularity Sensing. (June 2024).
- [50] Chenshu Wu, Feng Zhang, Beibei Wang, and KJ Ray Liu. 2020. mm-Track: Passive multi-person localization using commodity millimeter wave radio. In *IEEE INFOCOM 2020-IEEE Conference on Computer Communications*. IEEE, 2400–2409.
- [51] Kai Wu, Jacopo Pegoraro, Francesca Meneghello, J Andrew Zhang, Jesus O Lacruz, Joerg Widmer, Francesco Restuccia, Michele Rossi, Xiaojing Huang, Daqing Zhang, et al. 2024. Sensing in Bi-Static ISAC Systems with Clock Asynchronism: A Signal Processing Perspective. *IEEE Signal Processing Magazine* (2024).
- [52] Yaxiong Xie, Zhenjiang Li, and Mo Li. 2015. Precise Power Delay Profiling with Commodity WiFi (*MobiCom '15*). Association for Computing Machinery, New York, NY, USA, 53–64. <https://doi.org/10.1145/2789168.2790124>
- [53] Di Xiong, Junling Wang, Xiaoyang Qi, and Meiguo Gao. 2017. A coherent compensation method for multiband fusion imaging. In *2017 IEEE Radar Conference (RadarConf)*. IEEE, 1024–1027.
- [54] Jie Xiong, Karthikeyan Sundaresan, and Kyle Jamieson. 2015. Tone-Track: Leveraging Frequency-Agile Radios for Time-Based Indoor Wireless Localization. In *Proceedings of the 21st Annual International Conference on Mobile Computing and Networking (Paris, France) (MobiCom '15)*. Association for Computing Machinery, New York, NY, USA, 537–549.
- [55] Xin Yang, Jian Liu, Yingying Chen, Xiaonan Guo, and Yucheng Xie. 2020. MU-ID: Multi-user identification through gaits using millimeter wave radios. In *IEEE INFOCOM 2020-IEEE Conference on Computer Communications*. IEEE, 2589–2598.
- [56] Zhiyun Yao, Xuanzhi Wang, Kai Niu, Rong Zheng, Junzhe Wang, and Daqing Zhang. 2024. WiProfile: Unlocking Diffraction Effects for Sub-Centimeter Target Profiling Using Commodity WiFi Devices. In *Proceedings of the 30th Annual International Conference on Mobile Computing and Networking (Washington D.C., DC, USA) (ACM MobiCom '24)*. Association for Computing Machinery, New York, NY, USA, 185–199.
- [57] Youwei Zeng, Dan Wu, Jie Xiong, Jinyi Liu, Zhaopeng Liu, and Daqing Zhang. 2020. MultiSense: Enabling multi-person respiration sensing with commodity WiFi. *Proceedings of the ACM on Interactive, Mobile, Wearable and Ubiquitous Technologies* 4, 3 (2020), 1–29.
- [58] Youwei Zeng, Dan Wu, Jie Xiong, Enze Yi, Ruiyang Gao, and Daqing Zhang. 2019. FarSense: Pushing the range limit of WiFi-based respiration sensing with CSI ratio of two antennas. *Proceedings of the ACM on Interactive, Mobile, Wearable and Ubiquitous Technologies* 3, 3 (2019), 1–26.
- [59] Andrew Zhang, Md Lushanur Rahman, Xiaojing Huang, Yingjie Jay Guo, Shanzhi Chen, and Robert W Heath. 2020. Perceptive mobile networks: Cellular networks with radio vision via joint communication and radar sensing. *IEEE Vehicular Technology Magazine* 16, 2 (2020), 20–30.
- [60] Chaoyue Zhang, Zhiwen Zhou, Huizhi Wang, and Yong Zeng. 2023. Integrated super-resolution sensing and communication with 5G NR waveform: Signal processing with uneven CPs and experiments. In *2023 21st International Symposium on Modeling and Optimization in Mobile, Ad Hoc, and Wireless Networks (WiOpt)*. IEEE, 681–688.

- [61] Feng Zhang, Chenshu Wu, Beibei Wang, and K. J. Ray Liu. 2021. mm-Eye: Super-Resolution Millimeter Wave Imaging. *IEEE Internet of Things Journal* 8, 8 (2021), 6995–7008.
- [62] Huan Huan Zhang and Ru Shan Chen. 2014. Coherent processing and superresolution technique of multi-band radar data based on fast sparse Bayesian learning algorithm. *IEEE Transactions on Antennas and Propagation* 62, 12 (2014), 6217–6227.
- [63] J Andrew Zhang, Fan Liu, Christos Masouros, Robert W Heath, Zhiyong Feng, Le Zheng, and Athina Petropulu. 2021. An overview of signal processing techniques for joint communication and radar sensing. *IEEE Journal of Selected Topics in Signal Processing* 15, 6 (2021), 1295–1315.
- [64] J Andrew Zhang, Kai Wu, Xiaojing Huang, Y Jay Guo, Daqing Zhang, and Robert W Heath. 2022. Integration of radar sensing into communications with asynchronous transceivers. *IEEE Communications Magazine* 60, 11 (2022), 106–112.
- [65] Ying Zhang, Tingjing Wang, Huapeng Zhao, Yanxin Zhang, and Hua Zhao. 2017. Multiple radar subbands fusion algorithm based on support vector regression in complex noise environment. *IEEE Transactions on Antennas and Propagation* 66, 1 (2017), 381–392.
- [66] Hongzi Zhu, Yiwei Zhuo, Qinghao Liu, and Shan Chang. 2018. π -splicer: Perceiving accurate CSI phases with commodity WiFi devices. *IEEE Transactions on Mobile Computing* 17, 9 (2018), 2155–2165.